nature communications

Article

https://doi.org/10.1038/s41467-026-69600-z

Atmospheric CO_2 drawdown during the Emeishan flood basalt volcanism

Received: 3 July 2025

Accepted: 5 February 2026

Published online: 26 February 2026

Check for updates

Jiaheng Shen[1] ✉, Yi Ge Zhang[2], Dong-Xun Yuan[3] & Yi-Gang Xu[2]

The conventional model linking large igneous provinces (LIPs) to atmospheric CO_2 concentrations (pCO_2) predicts elevated CO_2 during volcanic emplacement, leading to biotic crises. However, this generalization requires testing. Here, we reconstruct pCO_2 variations throughout the Emeishan LIP emplacement (~260 Ma) using carbon isotopes from chlorophyll-derived compounds. Our high-resolution record reveals that pCO_2 declined from ~ 700 ppm to ~ 350 ppm during the early and main flood basalt phases, then increased during subsequent silicic eruptions. This pattern coincides with pre-eruptive crustal uplift driven by mantle plume impingement. We propose that CO_2 consumption associated with enhanced erosion and weathering of kilometer-thick Yangtze craton carbonates from regional uplift might have temporarily exceeded the CO_2 contribution from magmatic degassing. This is supported by geochemical data indicating that the Emeishan basalt is particularly CO_2-poor. Our findings demonstrate that LIP environmental impact begins before the main eruptive phase, highlighting that tectonic-magmatic interactions can produce more complex CO_2 patterns than previously recognized. This may explain why some LIPs caused extinctions, whereas others did not.

Large igneous provinces (LIPs) represent the most extensive volcanic events in Earth's history, typically outpouring over 100,000 cubic kilometers of lava within a short duration of 1 to 5 million years[1]. The conventional model links LIP volcanism to massive carbon dioxide (CO_2) emissions that drive global warming and environmental perturbations[2,3]. However, recent studies reveal that the relationship between LIP emplacement and atmospheric CO_2 is more complex. In the Central Atlantic Magmatic Province, episodic eruptions produce immediate CO_2 spikes, followed by declines attributed to enhanced weathering of freshly exposed volcanic rocks[4]. However, in the case of the Deccan Traps and Columbia River Basalt Group, CO_2 emissions are observed to increase prior to the onset of their main flood basalt volcanism due to the pre-eruption intrusions[5]. Moreover, "cryptic" carbon emissions can persist for several million years after the main eruptive phase through sustained magmatic degassing and metamorphism of organic-rich sediments[6]. These varying patterns might reflect differences in magma volatile content, intrusive activity, crustal architecture, and the relative timing of competing processes, such as volcanic degassing and enhanced weathering.

The environmental impact of LIPs was particularly significant during the Permian Period, which experienced two distinct biotic crises. The end-Guadalupian event (~260 million years ago (Ma)) was a critical precursor that possibly set the stage for the devastating end-Permian mass extinction[7,8]. This event notably affected shallow-marine taxa such as fusulines, corals and brachiopods across the Guadalupian-Lopingian (G-L) boundary[9–13]. Geochronological data have established temporal synchronicity between the end-Guadalupian mass extinction and the emplacement of Emeishan LIP[14–18]. While volcanogenic CO_2 has been hypothesized as the key driver of this biotic crisis[19], the actual relationship between the Emeishan volcanism and atmospheric CO_2 concentrations (pCO_2) remains poorly constrained.

Here we present a high-resolution pCO_2 record spanning the Mid to Late Permian using compound-specific carbon-isotope measurements of chlorophyll-derived biomarkers. By resolving pCO_2 changes

[1]School of Earth and Space Sciences, Peking University, Beijing, China. [2]State Key Laboratory of Deep Earth Processes and Resources, Guangzhou Institute of Geochemistry, Chinese Academy of Sciences, Guangzhou, China. [3]School of Resources and Geosciences, China University of Mining and Technology, Xuzhou, Jiangsu, China. ✉e-mail: jiahengshen@pku.edu.cn

through different phases of the Emeishan LIP development, we evaluate whether this volcanic episode conforms to the conventional LIP–CO_2 rise–extinction model, and how carbon cycle dynamics during this interval may have influenced the end-Guadalupian biotic crisis.

Results and Discussion

Carbon isotopic records of bulk sediment and phytane

High-resolution stable carbon isotope records of bulk sediments ($\delta^{13}C_{carb}$, $\delta^{13}C_{org}$) and biomarker phytane ($\delta^{13}C_{phy}$) (Fig. 1) from exposed strata at Shangsi section (32°20′ N, 105°28′ E, Supplementary Fig. 1) document well-preserved marine sedimentation spanning from the Guadalupian (including the Roadian, Wordian, and Capitanian stages) to the Lopingian. One characteristic signature of G-L boundary sections is the negative carbon isotope excursion (CIE) recorded in carbonates across various regions (Supplementary Fig. 2), although localized depositional hiatuses may obscure this trend. Our $\delta^{13}C_{carb}$ profile shows a gradual negative shift from ~4‰ to a minimum of ~1‰ during the transition from the Guadalupian to the Lopingian (Fig. 1c), followed by a return to pre-CIE levels (average of 4‰) during the Wuchiapingian stage. However, the $\delta^{13}C_{org}$ record exhibits a different pattern (Fig. 1d). At the G-L boundary, instead of a negative excursion, the values reach a transient maximum of ~ −23‰. This is followed by two distinct negative shifts throughout the Wuchiapingian stage, each interrupted by a temporary positive excursion.

Phytane is a diagenetic product derived from the phytol side chain of chlorophyll produced by photoautotrophic organisms, primarily algae and cyanobacteria[20]. The carbon isotopic composition of phytane preserves information about isotopic fractionation that occurred during photosynthetic carbon fixation by the primary producers that synthesized the original chlorophyll molecules. Consequently, the compound-specific $\delta^{13}C$ values of sedimentary phytane can serve as an effective proxy for reconstructing geological pCO_2 levels when appropriately calibrated[21–24]. At Shangsi, our $\delta^{13}C_{phy}$ measurements show a positive shift from ~ −31‰ to −27‰ from the Capitanian into the Early Wuchiapingian, followed by a gradual decrease to a minimum of ~ −32‰ (Fig. 1e). When converting $\delta^{13}C_{phy}$ values to the original biomass $\delta^{13}C$, we applied the established 3.3‰ enrichment factor documented by ref. 22. This correction accounts for the systematic isotopic fractionation that occurs during chlorophyll biosynthesis and subsequent diagenetic transformation to phytane.

To reconstruct atmospheric CO_2 levels, we quantified the isotopic fractionation (ε_p) associated with carbon fixation during photosynthesis using our paired values of $\delta^{13}C_{phy}$ and $\delta^{13}C_{carb}$ following established methods[25] (See Methods). This parameter increases systematically with rising pCO_2, though it can also be influenced by factors such as phytoplankton growth rate, cell geometry, and active carbon transport mechanisms[26–28]. In Fig. 1f, the calculated ε_p profile shows a negative shift from ~22‰ to a minimum of ~17‰ during the transition from the Capitanian to the onset of the Wuchiapingian, followed by a pronounced increase in ε_p. By the mid-Wuchiapingian stage, ε_p reaches a maximum value of ~24‰, and subsequently decreases to ~21‰.

Estimates of atmospheric pCO_2

New geochronological data provide a precise temporal framework of the eruption sequence within the Emeishan volcanic province[14–17]. The main eruptive phase of the Emeishan flood basalt volcanism occurred from 260.55 Ma to 259.1 Ma (refs. 15,17), with the earliest documented eruption at ca. 263.5 Ma (ref. 14). The waning stage of Emeishan LIP volcanism extended until ca. 257.4 Ma in the early Wuchiapingian[16].

Our ε_p-based estimates of pCO_2 (Fig. 2e) show that CO_2 concentrations remain stable at approximately 700 parts per million by volume (ppm) throughout the Roadian and Wordian stages. Coincident with the onset of the Capitanian stage, pCO_2 values begin to decrease at ~263.5 Ma, reaching an estimated minimum of 369 ppm, with a running mean average of ~550 ppm across the G-L boundary. This interval of decreasing pCO_2, from ~263.5 to 259.1 Ma, temporally corresponds with the early and main phases of the Emeishan flood

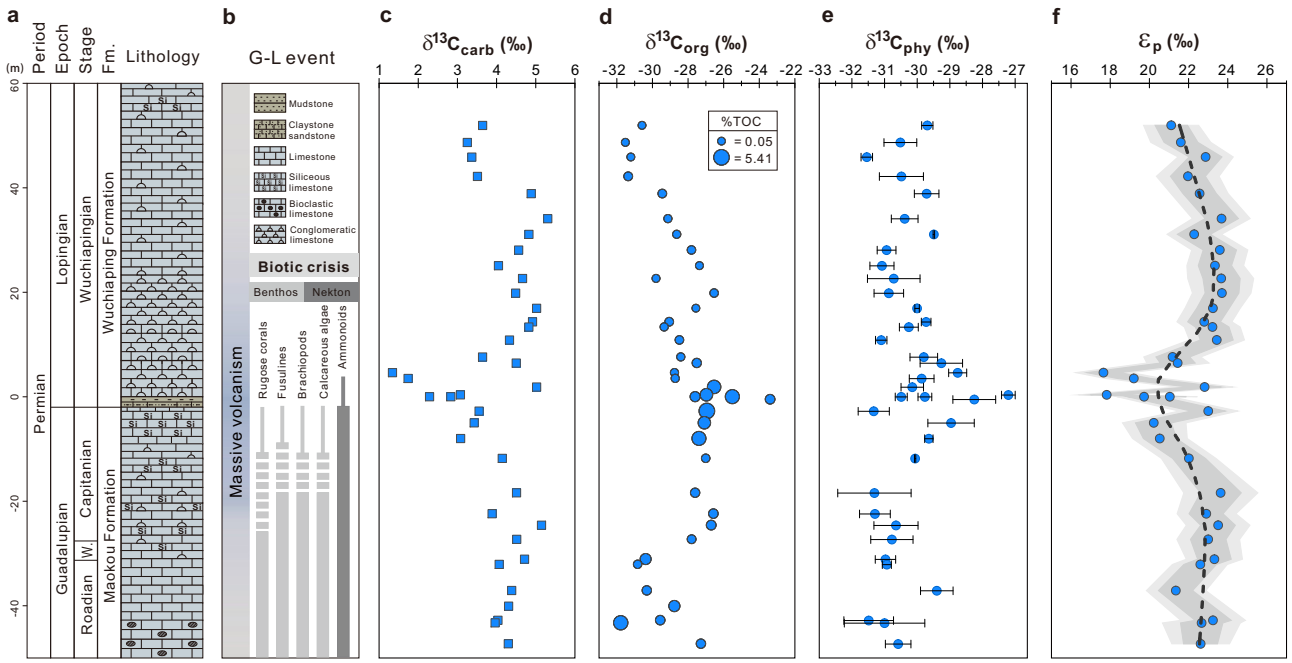

Fig. 1 | Guadalupian-Lopingian transitional interval chronology, stable isotope, and lipid biomarker stratigraphic records from Shangsi Section, China. **a** Chrono- and lithostratigraphy. **b** Geological and biological events from refs. 12–14. **c** Carbonate carbon isotopic compositions ($\delta^{13}C_{carb}$, blue squares). **d** Bulk organic carbon isotopic compositions ($\delta^{13}C_{org}$) together with %TOC (blue circles, size of symbol proportional to %). **e** Phytane carbon isotopic compositions ($\delta^{13}C_{phy}$, blue circles). Horizontal error bars represent 1σ of the mean ($n = 2$). **f** ε_p (blue circles) calculated from $\delta^{13}C_{phy}$ and $\delta^{13}C$ of dissolved CO_2 determined from (**c**). Shaded gray areas represent 68% (dark gray) and 95% (light gray) confidence intervals of ε_p calculation based on Monte Carlo simulations with 10,000 times (See Methods). Black dashed line represents the LOESS smoothing function (See Methods). Data in Supplementary Table 1. Fm Formation, W Wordian.

https://doi.org/10.1038/s41467-026-69600-z

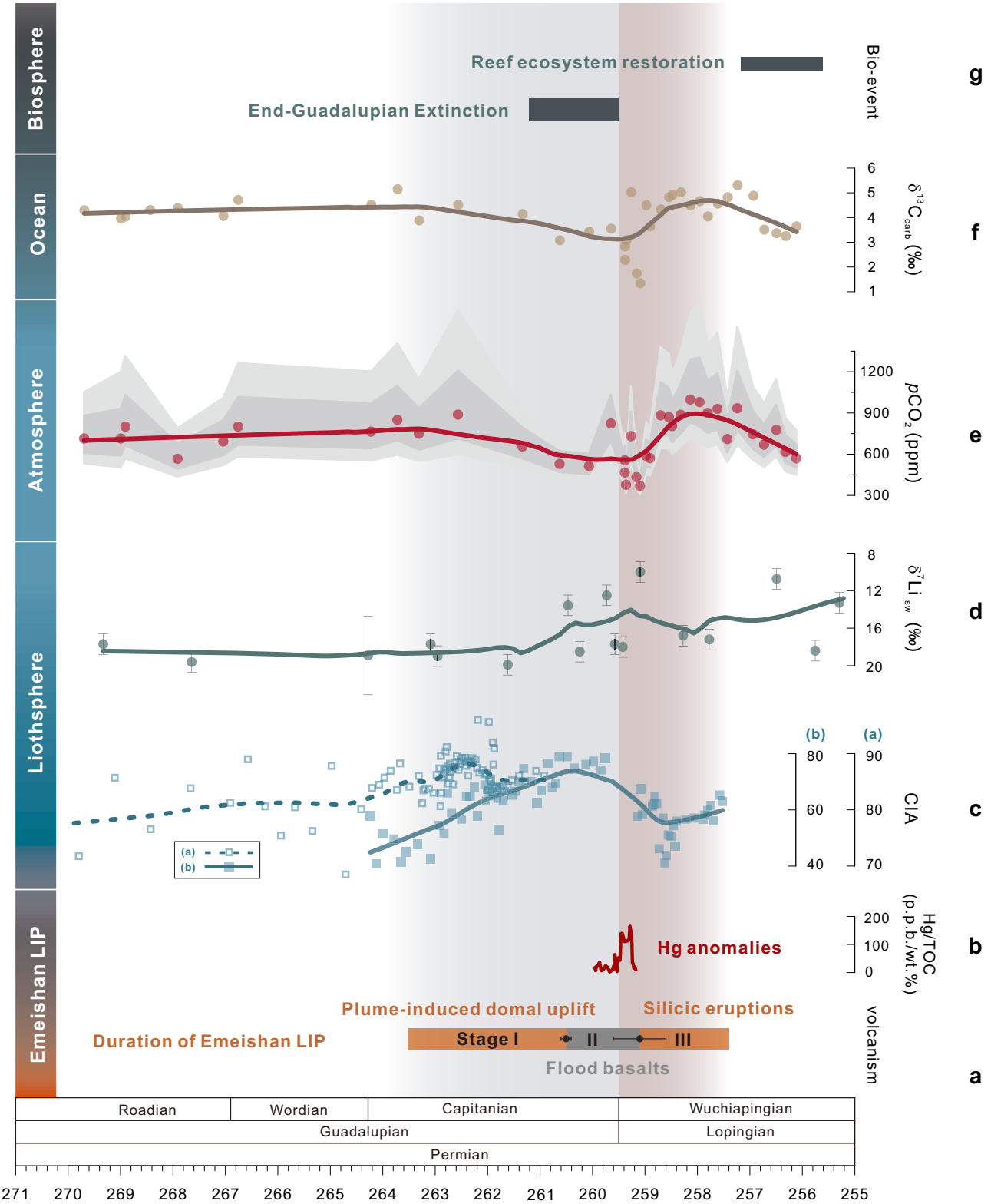

Fig. 2 | Estimates of atmospheric CO_2 and major geological events associated with the Emeishan LIP spanning from the Guadalupian to the Lopingian. **a** Evolutionary stages and high-precision chronology of the Emeishan LIP. Data from refs. 14–17. **b** Mercury record (Hg/TOC) for the timing and strength of volcanism[19]. **c**, **d** The degree of continental weathering based on (**c**) chemical index of alteration (CIA) and **d** seawater lithium isotope (δ^7Li_{sw}) records[38–40]. **e** pCO_2 estimates based on ε_p. Shaded gray areas represent 68% (dark gray) and 95% (light gray) confidence intervals of pCO_2 estimation based on Monte Carlo simulations (See Methods). **f** Carbonate carbon isotopic compositions ($\delta^{13}C_{carb}$) from this study. **g** Biological events from refs. 14,57,104. Solid and dashed lines in (**c**–**f**) represent the LOESS smoothing function.

basalt volcanism (Fig. 2a, e). Counterintuitively, the minimum pCO_2 level coincides with the termination of the main phase of flood basalt eruptions, after which pCO_2 values increase despite reduced eruption volumes. This surprising relationship is further highlighted by the correspondence between lowest pCO_2 values and peak mercury (Hg) anomalies[19] (Fig. 2b), demonstrating that the most intense volcanic activity during the main eruption phase paradoxically resulted in atmospheric CO_2 drawdown rather than the expected increase. In the Early Wuchiapingian, pCO_2 value reaches an estimated maximum of 1000 ppm, with a running mean average of ~900 ppm. This interval of elevated CO_2 level coincides with explosive silicic eruptions rather than the earlier flood basalt volcanism[16,29]. Following the termination of the Emeishan volcanism, the pCO_2 values decrease to approximately 600 ppm.

Our observed pCO_2 trend from the Emeishan LIP reveals several unexpected findings in carbon cycle behavior that fundamentally challenge conventional understanding of LIP-climate interactions. First, while the standard model predicts atmospheric CO_2 increases during peak flood basalt volcanism[4], the Emeishan LIP exhibits precisely the opposite trend: a sustained CO_2 decrease from ~700 to ~350 ppm during its most intense volcanic phase. This decoupling between volcanic activity and atmospheric CO_2 is further highlighted by the correspondence between minimum pCO_2 values and peak Hg anomalies, demonstrating that the most vigorous eruption phase paradoxically coincided with maximum carbon drawdown rather than addition. Second, our data reveal that the negative CIE at the G-L boundary occurred alongside CO_2 drawdown rather than increase, contrasting with the typical coupling between negative CIEs and CO_2 spikes observed in numerous other environmental perturbations throughout Earth history[23,30,31]. Third, the subsequent CO_2 increase during the later silicic eruptive phase—despite its lower eruption volume—further demonstrates that eruption intensity does not directly correlate with atmospheric CO_2 response in this case, reversing the expected pattern of volcanogenic carbon forcing. These multiple discrepancies from established patterns collectively indicate that a distinct and previously unrecognized mechanism must have dominated the carbon cycle during the Emeishan event, effectively counterbalancing and even overwhelming the expected volcanic CO_2 contributions.

Mantle plume-driven uplift and carbonate weathering as a carbon sink

The key to understanding the paradoxical CO_2 pattern during the Emeishan LIP lies in the unique tectonic processes and geomorphological changes that preceded the main volcanic eruptions. Unlike many other LIPs, the Emeishan event was characterized by extensive pre-eruptive crustal doming and uplift that fundamentally altered regional weathering dynamics[32–34]. Biostratigraphic and sedimentological studies of 67 sections within the Middle Permian Maokou Formation, beneath the Emeishan basalts in South China, provide compelling evidence of this uplift. These studies document systematic thinning of the Maokou strata toward the center of the province and widespread development of unconformities that become increasingly prominent approaching the center of the domal structure (Supplementary Fig. 3). The observed pattern of stratigraphic thinning outlines a subcircular uplifted area with a radius of approximately 800 km that experienced uplift of up to 1000 m[32] (Fig. 3). This uplift, estimated to have lasted approximately 3 million years, is consistent with theoretical models of lithospheric response to mantle plume impingement[35–37].

The critical environmental consequence of this uplift was the exposure of vast expanses of previously submerged marine carbonates to subaerial weathering conditions. The development of extensive paleoweathering crusts, paleosols, and karst topography at the unconformity between the Maokou Formation and overlying Emeishan basalts provides direct evidence for intensified weathering during this period. This enhanced weathering is further corroborated by geochemical proxies, including a substantial decline in seawater lithium isotopes (δ^7Li_{sw})[38] (Fig. 2d) and elevated Chemical Index of Alteration (CIA) values[39,40] (Fig. 2c), both reliable indicators of increased continental weathering intensity.

In addition, the distinctive CO_2 record of the Emeishan LIP is closely linked to its broader Late Paleozoic weatherability context. Marcilly et al. (ref. 41) reconstruct high-weatherability zones (HWZ) from climatically sensitive lithologies and highlight their importance for the evolution of the Late Paleozoic Ice Age (LPIA). During the Permian, HWZ preferentially shifted toward the China blocks and Siberia rather than the arid central Pangean interior[41], placing South China within a warm, high-runoff belt conducive to strong CO_2 uptake. In such low-latitude settings, tectonic uplift can shift weathering from supply-limited to kinetically controlled regimes and thereby enhance CO_2 consumption[42]. Within this framework, plume-related doming above Emeishan would have amplified weathering of the rapidly exposed Yangtze carbonate platform, producing a pronounced CO_2 drawdown. Therefore, our Emeishan record reflects a focused, characteristic, plume-amplified weathering pulse operating within global LPIA-scale changes in weatherability.

Carbonate weathering is typically not considered a major driver of long-term atmospheric CO_2 changes because it operates on relatively short timescales with a balanced carbon budget—CO_2 consumed during weathering is largely released during subsequent carbonate precipitation in the oceans (e.g., GEOCARB III[43]). Under steady-state conditions, the net effect on atmospheric CO_2 is minimal. However, the Emeishan scenario represents a departure from this steady-state scenario. The rapid and extensive uplift of carbonate platforms created a transient but powerful carbon sink by dramatically increasing the weathering flux over approximately 3 million years—a timeframe long enough to constantly impact pCO_2 levels but short enough to prevent full compensation through the carbonate burial feedback system.

Notably, the Late Permian predates the Mid-Mesozoic proliferation of pelagic calcifiers and the establishment of a well-buffered deep-sea carbonate sink. In such a 'Neritan' ocean state, carbonate burial was dominated by platforms and shelves, and the negative feedback associated with deep-sea carbonate compensation was inherently weaker and slower[44]. Consequently, a large, transient alkalinity–DIC injection from the rapid exposure and weathering of the Maokou carbonates would not have been effectively buffered by pelagic dissolution or precipitation. This inefficiency likely produced a stronger atmospheric pCO_2 response than in the modern ocean, sustaining pCO_2 drawdown on Myr timescales and amplifying the climatic consequences of enhanced carbonate weathering during the crustal doming of the Emeishan LIP. This Permian carbon-cycle architecture strengthens the plausibility of our interpretation that tectonic uplift may have dominated the atmospheric signal across the Emeishan LIP interval.

Quantitatively, this uplifted carbonate province had a substantial weathering potential. Assuming the uplifted area extended across a circular region with an 800 km radius and experienced average erosion of 150 m thickness[32], we estimate ~754,000 Gt of limestone was subjected to weathering, based on an average limestone density of 2.5×10^{12} kg/km^3. This erosion would have mobilized ~90,480 Gt of inorganic carbon and 9500 Gt of organic carbon (see Methods), resulting in a net consumption potential of 80,980 Gt C from the atmosphere. This value substantially exceeds the estimated contemporary atmospheric CO_2 reservoir of ~1480 Gt C, based on the initial concentration of 700 ppm during the Roadian and Wordian stages (see Methods). Even if marine carbonate compensation and buffering mechanisms limited the atmospheric impact to only 10% of the weathering flux (~8098 Gt C), this still exceeds the entire atmospheric carbon reservoir, demonstrating the enormous potential of this mechanism to drive significant CO_2 drawdown.

https://doi.org/10.1038/s41467-026-69600-z

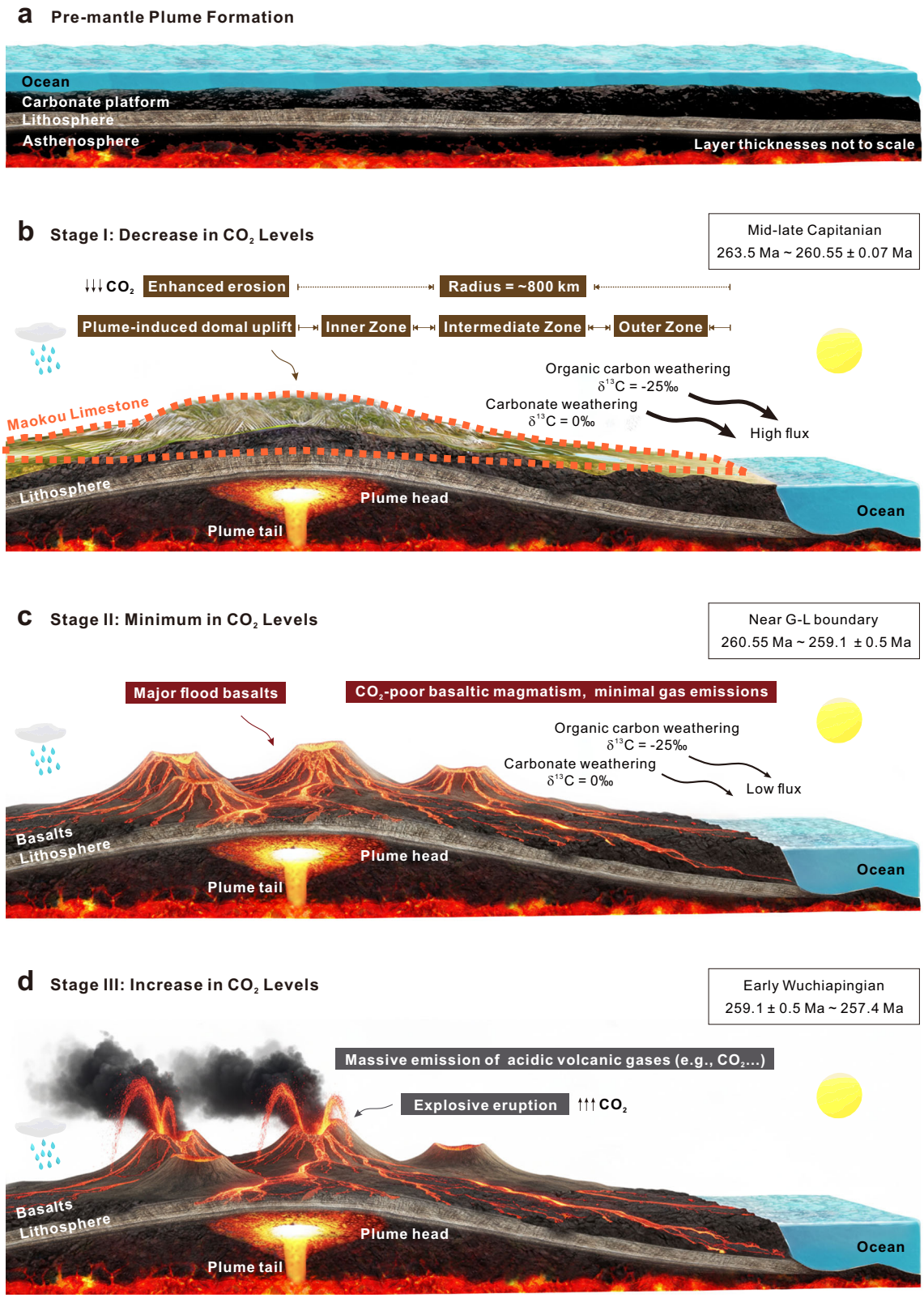

Fig. 3 | Time series and evolutionary stages of Emeishan LIP emplacement, and the carbon cycle spanning from the Guadalupian to the Lopingian. a Stable carbonate platform prior to the mantle plume formation. **b** Kilometer-scale crustal uplift and erosion due to the Emeishan mantle plume during the Stage I, with the orange dashed area representing the weathered Maokou Formation, leading to the decrease of CO_2. **c** The main eruption of the Emeishan flood basalts during the Stage II, with CO_2-poor basaltic magmatism and low CO_2 levels. **d** Emeishan silicic eruptions and associated greenhouse gas emissions (e.g., CO_2) during the Stage III. The widths of the curved arrows with isotopic signals in (**b**, **c**) represent the magnitude of carbon flux. Note that the thicknesses of Earth's internal layers in this figure are not to scale. This figure is intended as a conceptual illustration and does not reproduce the full geometry or complexity of the LIP.

This large-scale weathering of carbonate platforms represents a powerful carbon sink that could readily overwhelm concurrent volcanic CO_2 emissions, particularly given the distinctive geochemical composition of the Emeishan basalts. Analyses of the volatile content in Emeishan volcanic rocks provide critical context for understanding this carbon cycle dynamic. Tang et al. (ref. 45) conducted comprehensive geochemical and isotopic analyses of volatiles in Emeishan picrites and basalts, using both bulk-rock measurements and studies of melt inclusions trapped in olivine phenocrysts. These investigations revealed that Emeishan basalts contain remarkably low CO_2 concentrations, averaging only ~135 ppm. This is dramatically lower than typical ocean island basalt values of 6500–28,000 ppm and much less than other continental flood basalts associated with major extinction events. Note that the value of 135 ppm is lower than typical values observed in modern systems and may have been affected by loss during preservation. Therefore, this value should be interpreted with caution as a direct quantitative measure of magmatic degassing. Nevertheless, it provides strong comparative evidence that the Emeishan basaltic magmatism was notably low in CO_2 and that degassing was not primarily magmatic.

The relatively CO_2-poor nature of the Emeishan basalts stands in stark contrast to other LIPs like the Siberian Traps, which have been associated with massive carbon emissions during the end-Permian mass extinction. Isotopic analyses of helium and carbon in the Emeishan basalts indicate they were derived from a relatively degassed mantle source, from which much of their volatile content had been depleted prior to the eruption. Beyond the magmatic volatile budget, thermogenic CO_2 generated where sills intrude organic-rich sedimentary basins can be both volumetrically significant and rapid[46–50]. In the Siberian Traps, high-precision geochronology documents a transition from early extrusive lavas/pyroclastics to widespread sill emplacement into the volatile-rich Tunguska Basin[51]. The emplacement of these spatially extensive sills led to enormous thermogenic degassing[46–49]. An independent pCO_2 reconstruction[23] shows a coeval CO_2 rise with the onset of this sill-dominated intrusive phase in the Siberian Traps, supporting this interpretation. In contrast, the Emeishan LIP is characterized by layered mafic intrusions concentrated in the inner-zone Panxi region[52–54] (see Methods for discussion of intrusive activity). Comparable province-wide sill intrusion into organic-rich sedimentary sequences analogous to those in the Tunguska Basin has not been demonstrated in the Emeishan LIP. The predominance of carbonate host rocks and associated contact aureoles around Emeishan intrusions suggests that metamorphic carbon liberated by decarbonation of carbonate country rocks was likely the main degassing source[55]. However, the limited precision of existing age data for Emeishan intrusions hinders precise constraints on the relative contribution and timing of thermogenic CO_2 release. Nevertheless, because intrusions are confined to the inner zone, their impact on atmospheric CO_2 was likely limited. Therefore, the combination of enhanced weathering capacity and relatively CO_2-poor magmatism created conditions whereby carbon sequestration would dominate over volcanic degassing, even during periods of intense eruptive activity.

Isotopic response and carbon cycle implications

The large-scale carbonate weathering triggered by pre-eruptive uplift not only affected atmospheric CO_2 levels but also left a distinctive signature in the carbon isotope record. To evaluate the isotopic implications of this mechanism, we applied a mass balance approach to quantify the expected $\delta^{13}C$ shifts resulting from enhanced carbonate weathering. The weathering of the Maokou Formation would have introduced a substantial amount of carbon with distinctive isotopic signatures into the global carbon cycle. Using a mass balance calculation, we estimated the integrated $\delta^{13}C$ value of the weathering input. Assuming average $\delta^{13}C$ values of 0‰ for the weathered carbonate component (typical of marine carbonates) and −25‰ for the organic carbon component (with an average TOC of 1.26% derived from Maokou Formation samples), the composite weathering input would have a $\delta^{13}C$ value of approximately −2.38‰ (see Methods). This represents a significantly ^{13}C-depleted flux compared to the background marine carbonate values of approximately +1‰ recorded before the excursion.

Under a hypothetical scenario without oceanic buffering or carbonate compensation, the input of 99,980 Gt C with $\delta^{13}C$ value of −2.38‰ into the ocean-atmosphere system would result in a new ocean $\delta^{13}C$ value of −1.39‰. This would produce a negative excursion in marine carbonate $\delta^{13}C$ of about 2.39‰ (from +1‰ to −1.39‰) over the 3-million-year period of enhanced weathering. In a more realistic scenario incorporating carbonate compensation, where for every mole of CO_2 added from weathering, approximately 0.8 moles of carbonate sediment dissolves, the expected shift would be moderated to about 1.28‰, with a new equilibrium $\delta^{13}C$ value of −0.28‰.

The magnitude of these calculated isotopic shifts aligns remarkably well with our observed CIE at the G-L boundary, where $\delta^{13}C$ values decline from ~4‰ to ~1‰ (Fig. 1c). This coherence between our theoretical calculations and the actual isotopic record provides independent validation of the weathering mechanism we propose. Importantly, the timing of this negative excursion coincides precisely with the interval of decreasing atmospheric CO_2, supporting our interpretation that both signals reflect the same underlying process of enhanced weathering.

This isotopic pattern represents another distinctive feature of the Emeishan LIP compared to other major volcanic episodes. Typically, negative CIEs associated with LIPs are interpreted as evidence for massive injections of isotopically light carbon into the atmosphere, often accompanied by warming and ocean acidification. In the Emeishan case, however, the negative CIE occurs alongside CO_2 drawdown rather than an increase, demonstrating that different carbon-cycle mechanisms were involved. This pattern further emphasizes the unique nature of the Emeishan event and underscores the importance of considering the full geological context—including pre-eruptive processes—when interpreting carbon-cycle perturbations associated with LIPs.

Our findings challenge the conventional model linking LIPs directly to CO_2 increases and global warming. The Emeishan case demonstrates that pre-eruptive mantle-lithosphere interactions can drive carbon-cycle perturbations millions of years before the first lava flows, potentially triggering atmospheric responses opposite to traditional expectations. More broadly, the climatic expression of LIP volcanism is shaped by a combination of factors, including emplacement style (extrusive vs. intrusive), mantle volatile loading, lithospheric structure, paleogeography, and the prevailing ocean–carbon state, etc. The Emeishan LIP developed in a tropical, high-weatherability setting, where crustal uplift exposed kilometer-thick Yangtze platform carbonates to intense erosion and weathering under a Late Paleozoic ocean characterized by weak pelagic buffering, while the associated basaltic magmatism was notably CO_2-poor. Together, these factors explain why the Emeishan LIP is distinct among continental flood basalts in exhibiting pCO_2 decline during the main basaltic phase. This fundamentally reframes how we understand deep Earth-surface environment connections, suggesting that a LIP's environmental impact follows more complex pathways than previously recognized, potentially explaining why some LIPs are linked to mass extinctions, whereas others are not. The distinctive CO_2 drawdown pattern we observe emphasizes the importance of examining each LIP within its complete geological context rather than applying a universal template. Future research should adopt an integrated Earth System approach that examines the full sequence of mantle-to-atmosphere interactions across all stages of LIP development—crucial for accurately interpreting cause-and-effect relationships between volcanism and environmental change throughout Earth's history.

Methods

Materials

Samples were collected from the Shangsi section (32°20′ N, 105°28′ E, Supplementary Fig. 1), Shangsi Village, Guangyuan City, Sichuan Province, China. The Shangsi section, a prominent candidate for the Global Stratotype Section and Point (GSSP) of the Permian-Triassic boundary, is distinguished by its well-exposed marine successions and extensive research foundation. Based on paleogeographic reconstruction, Shangsi was located in the eastern region of the Paleo-Tethys during the Middle to Late Permian. All samples were collected from outcrops where the surface layers had been completely removed, exposing fresh layers to avoid weathered or otherwise contaminated rocks. Stratigraphically, the Shangsi section includes the Maokou and Wuchiaping formations, which correspond to the Guadalupian and Lopingian series, respectively. The G-L boundary is placed at the base boundary of the Wuchiaping Formation[56]. Fossil records indicate that the end-Guadalupian extinction was a multi-phase biotic crisis characterized by a gradual decline in biodiversity and episodic turnovers beginning in the mid-Capitanian. It affected multiple taxonomic groups such as fusulines, corals, ammonoids, brachiopods, conodonts and bivalves, leading to widespread ecosystem collapse[9–13].

Chronology

The age control for the G-L interval is derived from the latest high-precision geochronology. The tie-points are as follows: 273.01 ± 0.14 Ma for the base of the Roadian[57], 266.9 ± 0.4 Ma for the base of the Wordian[58], 264.28 ± 0.16 Ma for the base of the Capitanian[58], 259.51 ± 0.21 Ma for the base of the Wuchiapingian[59] and 254.14 ± 0.07 Ma for the base of the Changhsingian[60].

Intrusive activity during the Emeishan LIP emplacement

The Emeishan intrusive system is expressed by a cluster of layered mafic-ultramafic complexes in the inner zone, typically surrounding the Panxi area (Panzhihua-Xichang, Supplementary Fig. 3a), including Panzhihua, Baima, Hongge, Taihe, Binggu and Xinjie[18,52–54,61]. Geophysical imaging along a seismic profile crossing the Emeishan LIP shows that crustal thickening and magmatic modification are most pronounced in the inner zone, where a thick mafic underplating layer is present, whereas the intermediate and outer zones lack comparable underplating features, implying that magmatic intrusion in these zones was relatively limited[62]. To date, only a single field study has documented composite, zoned diabase sills occurring in the outer zone, at Luodian in southern Guizhou[63]. Overall, the prevailing view on the distribution of intrusions in the Emeishan LIP is that they are mainly concentrated in the inner zone.

The timing of the Emeishan LIP intrusions broadly overlaps the main basaltic eruptions and extends from the earliest magmatic records to the waning stage (Supplementary Fig. 3d; refs. 14–18,52–54,61,63,64). Although the current consensus is that Emeishan LIP extrusive and intrusive activities were essentially coeval, the analytical quality and precision of available age determinations for the intrusions are insufficient to establish a precise intrusive chronology comparable to that of the Siberian Traps.

The country rocks intruded by the Emeishan bodies are predominantly carbonates. In the inner zone, intrusions were emplaced largely into Neoproterozoic (Sinian) dolostones that are nearly pure (containing very little clay or quartz), interbedded with siliceous limestones, marlstones and minor shales of the Dengying Formation[65]. In the outer zone, the Luodian sills intrude Early-Middle Permian Sidazhai Formation carbonates[63]. The development of contact aureoles within these carbonate successions suggests metamorphic decarbonation and localized carbonate partial melting of the country rocks during emplacement[65,66].

Sample cleaning and preparation

All rock samples were cleaned and prepared following procedures described in ref. 67. Specifically, the rock samples were sonicated in three solvents (methanol, dichloromethane, and n-hexane) to remove any organic contamination. After cleaning, the samples were crushed into fine powder using a ring and puck mill and then stored in pre-combusted glass jars.

Bulk isotopic analysis

Bulk carbon isotopic values of carbonate ($\delta^{13}C_{carb}$) were analyzed using a Thermo Scientific GasBench coupled with a Delta V Plus isotope ratio mass spectrometer (IRMS), with Chinese national standards, GBW 04416 and GBW 04417 as references, at the Institute of Geology and Geophysics, Chinese Academy of Sciences. The carbon isotopic ratios are reported using standard δ notation ($\delta^{13}C$ in ‰) relative to Vienna Pee Dee Belemnite (VPDB). Standard precision is better than 0.05‰ (1σ).

Rock powders were completely decarbonated by reacting with dilute hydrochloric acid and subsequently rinsed with Barnstead Nanopure water until the pH was neutral. Bulk carbon isotopic values of organic matter ($\delta^{13}C_{org}$) were analyzed using a Thermo Scientific Flash elemental analyzer (EA) coupled with a Delta V Plus IRMS, with in-house laboratory standards along with reference standards IAEA-600 and USGS 40, at the Institute of Geology and Geophysics, Chinese Academy of Sciences. All samples were measured in triplicate. Standard precision is better than 0.1‰ (1σ).

Lipid extraction and biomarker analysis

Samples were extracted using a Thermo Scientific™ Dionex™ ASE™ 350 Accelerated Solvent Extractor in 9:1 dichloromethane/methanol mixture at 100 °C to obtain total lipid extracts (TLEs). To maximize biomarker yield, more than 150 g of powdered rock was used per sample for extraction, and three ASE extraction cycles were performed until the extract color became lighter, ensuring sufficient biomarker abundance for subsequent isotopic analyses. Biomarker analysis was conducted at the Stable Isotope Geoscience Facility, Texas A&M University and the Institute of Urban Environment, Chinese Academy of Sciences. Saturated hydrocarbons were eluted through SiO_2-gel chromatography with 100% hexane. To remove *n*-alkanes, these fractions were transferred to cyclohexane and treated with activated 5Å molecular sieves at 85 °C for 24 h. Before isotopic analysis, we verified phytane identity and purity by GC-MS and required baseline-resolved phytane peaks with good peak shape. Any chromatogram showing peak overlap (coelution) was excluded. Representative GC-MS chromatograms illustrating phytane identification and baseline separation are shown in Supplementary Fig. 7. Compound-specific isotopic compositions of phytane ($\delta^{13}C_{phy}$) were analyzed using a Thermo Trace Ultra gas chromatograph coupled with a MAT 253 IRMS, equipped with a HB-5 column (50 m × 0.2 mm × 0.33 μm) and a programmable temperature vaporization injector with helium as the carrier gas. The oven program was set at 60 °C upon sample injection, held for 1.4 min, then ramped up uniformly at 10 °C min^{-1} to 180 °C, 4 °C min^{-1} to 260 °C, and 20 °C min^{-1} to 320 °C, where it was held for 10 min. An external standard of n-alkanes with known $\delta^{13}C$ values (A7, Arndt Schimmelmann, Indiana University) was used to monitor the instrument's performance. The carbon isotopic ratios are reported relative to Vienna Pee Dee Belemnite. Hexadecane (C_{16}) or eicosane (C_{20}) with known $\delta^{13}C$ values was used as the internal standard. All samples were measured in duplicates and corrected for drift and linearity. Standard precision is better than 0.3‰.

Terrestrial organic matter input. To assess the contribution of terrigenous organic matter in the Shangsi samples, we used *n*-alkane and isoprenoid indices (Supplementary Table 2). The abundances of these compounds were determined using an Agilent 8890 gas chromatograph equipped with a flame ionization detector (GC-FID) and a

DB-5 capillary column (30 m × 0.25 mm × 0.25 μm). The temperature program started at 70 °C, then increased at a rate of 10 °C/min to 210 °C, followed by 3 °C/min to 300 °C, where it was held for 30 min. Based on peak areas, we calculated (*i*) the terrigenous-aquatic ratio (TAR; TAR = $[C_{27}+C_{29}+C_{31}]/[C_{15}+C_{17}+C_{19}]$), which contrasts long-chain (C_{27}–C_{31}) higher-plant wax alkanes with short-chain (C_{15}–C_{19}) algal/bacterial alkanes[68], (*ii*) the carbon preference index (CPI; CPI = $[C_{25}+C_{27}+C_{29}+C_{31}]/[C_{24}+C_{26}+C_{28}+C_{30}]$) of long-chain *n*-alkanes as an indicator of odd-over-even predominance typical of fresh higher-plant waxes[69,70], and (*iii*) pristane/phytane (Pr/Ph), which generally reflects redox and depositional setting[71]. At Shangsi, 33 out of 39 samples have TAR values below 1, with an average of 0.58 for these samples. The six samples with TAR values greater than 1 are not concentrated at any particular stratigraphic level but occur randomly throughout the section. Long-chain CPI values cluster around 1 (0.67–0.98; average = 0.89 ± 0.07, $n = 39$), and Pr/Ph ranges from 0.23–1.03 (average = 0.59 ± 0.14; $n = 38$), with no values exceeding 1.5. Together, these indices indicate that the organic matter in the Shangsi samples is primarily derived from aquatic/marine sources, with a relatively minor higher-plant contribution.

pCO_2 calculations

Phytane-based pCO_2 reconstructions rely on the measurements of carbon isotopic composition from both phytane ($\delta^{13}C_{phy}$) and associated carbonates ($\delta^{13}C_{carb}$). The carbon isotope fractionations (ε_p) during phytoplankton photosynthesis are utilized to reconstruct seawater and atmospheric CO_2 concentrations throughout the Phanerozoic era. ε_p values are derived from the $\delta^{13}C$ values of dissolved CO_2 (δ_d) and photosynthetic biomass (δ_p) (ref. 25). δ_p is calculated from the isotopic difference between phytol and photoautotrophic biomass. Prior culture studies estimate this difference to be 3.3 ± 1.3‰ (ref. 22). Meanwhile, δ_d is calculated from $\delta^{13}C_{carb}$, using the temperature-dependent relationship between the $\delta^{13}C$ values of dissolved CO_2 and solid carbonate[72,73]. The coeval seawater temperatures were derived from a compilation of high-resolution conodont apatite $\delta^{18}O$ records[57,74,75]. Given the varying sampling resolutions, a LOESS smoothing function was applied to derive continuous temperature data across the timeline. The 1σ (68%) and 2σ (95%) uncertainties in ε_p calculations were determined through Monte Carlo simulations that accounted for various sources of uncertainty, including analytical uncertainty in $\delta^{13}C_{phy}$, a standard deviation (SD) of 1.3‰ in the isotopic offset between phytane and biomass, and a 4 °C SD in seawater temperature estimation.

In pCO_2 reconstructions, it is assumed that dissolved CO_2 is primarily transported to the site of carbon fixation in photosynthetic cells by diffusion[76]. Carbon concentrating mechanisms (CCMs) were unlikely to be fully active during the relatively high CO_2 levels of the Permian and Triassic periods[22], as this active carbon uptake by CCMs requires substantial energy, a characteristic observed in many modern algae species[77]. The concentrations of aqueous CO_2 [CO_2(aq)] were calculated using the equation: $\varepsilon_p = \varepsilon_f - b/[CO_2(aq)]$, where ε_f represents the net kinetic isotope fractionation of cellular enzymatic processes, *b* represents the physiological factors[78–80]. In this study, ε_f was assigned a value of 28‰. The *b*-value was calculated using the equation: $b = 82.05 \times [PO_4^{3-}] + 86.28$, where the $[PO_4^{3-}]$ represents a phosphate concentration of 0.2 μM as a representative level. Further discussion on ε_f and *b*-value are discussed below. Finally, atmospheric pCO_2 concentrations were calculated from CO_2(aq) using Henry's law under the assumption of air-sea equilibrium[81]. The 1σ (68%) and 2σ (95%) uncertainties in pCO_2 calculations were determined through Monte Carlo simulations that accounted for various sources of uncertainty, including analytical uncertainty in $\delta^{13}C_{phy}$, a SD of 1.3‰ in the isotopic offset between phytane and biomass, a 4 °C SD in seawater temperature estimation, and uncertainty in $[PO_4^{3-}]$, which ranged from 0.17 to 0.27 μM.

Uncertainties in pCO_2 estimates

The calculation of pCO_2 involves various assumptions, including the dependence of term *b* on $[PO_4^{3-}]$ and the value of enzymatic isotope fractionation (ε_f), along with potential uncertainties in seawater temperature that can impact pCO_2 estimates. These factors are discussed below.

Estimates of *b*. In the process of photosynthetic carbon fixation, the parameter *b* synthesizes the effects of growth rate, cellular morphology, and membrane permeability on carbon isotopic discrimination. In this paper, we adopt the estimates for *b* utilized in previous CO_2 reconstructions for the Permian-Triassic boundary[23]. The refined equation for *b* as a function of $[PO_4^{3-}]$ is derived from sediment data and is expressed as $b = 82.05 \times [PO_4^{3-}] + 86.28$ (ref. 82). This formula yields *b* values that enhance the accuracy of CO_2 reconstructions, providing better alignment with sedimentary records. In this equation, we used a representative $[PO_4^{3-}]$ concentration of 0.2 μM at a depth of 20 m, representing the average value within the modern observed range of 0.17 to 0.27 μM from the ocean surface to a depth of 50 meters. Due to the absence of data on the temporal variability of *b*, we maintained it as a constant value throughout the study interval. Regardless of the uncertainty of *b*, its impact is confined to the absolute values of pCO_2, as sensitivity analysis demonstrates that pCO_2 changes by less than 6% when the maximum or minimum *b* values are applied (see Supplementary Fig. 4). Consequently, these variations do not alter the overall trend of pCO_2 calculations over time.

Estimates of ε_f. Enzymatic isotope fractionation (ε_f) is primarily driven by the activity of the enzyme Rubisco and/or contributions from β-carboxylases. Experimental studies on the growth of eukaryotic algae and cyanobacteria have determined that ε_f values typically are within the range of 25‰ to 28‰ (refs. 27,79,83,84). In this study, we adopt the ε_f value of 28‰, as β-carboxylation is typically inhibited under higher CO_2 levels, leading to larger ε_f value[85]. Supplementary Fig. 5 shows the theoretical relationship among ε_p, phosphate concentration, and seawater temperature, based on the ε_f value of 28‰.

A recent modern-ocean calibration of the phytol ε_p-[CO_2(aq)] relationship, based on a Deming regression, reports $\varepsilon_f \approx 23.9$‰ and $b \approx 82.4$ (ref. 24). This study refines and strengthens the phytol/phytane-based approach to pCO_2 reconstruction, thereby improving its reliability and expanding its applicability for future studies. In our study, the *b* value is parameterized from the phosphate relationship, which yields $b \approx 102$. This value is substantially lower than the traditional constant of $b = 170$ and broadly consistent with the low-*b* range in modern calibrations[24]. As for ε_f, while the modern calibration provides an important reference framework, several considerations suggest that its ε_f value may not be directly applicable to our study. First, the calibration domain of modern datasets is limited at the high-[CO_2(aq)] end. The open ocean rarely attains very high [CO_2(aq)], and near-shore waters, where [CO_2(aq)] can be higher, are typically excluded to minimize terrestrial inputs. This restriction reduces the opportunity to observe maximum fractionation, thereby leading to a lower fitted ε_f (ref. 24). Second, carbon-concentrating mechanisms (CCMs) and active HCO_3^- uptake (β-carboxylation) are pervasive in modern phytoplankton and tend to depress the apparent fractionation. During deep-time intervals, these pathways were likely down-regulated under elevated pCO_2, implying a higher effective ε_f. In addition, because of the asymptotic nature of the ε_p-pCO_2 relationship, adopting a low ε_f places more of our data near the $\varepsilon_p \approx \varepsilon_f$ limit, where small uncertainties in ε_p can propagate into disproportionately large pCO_2 (ref. 24). For these mechanistic and methodological reasons, we adopt $\varepsilon_f = 28$‰ in our pCO_2 reconstructions.

Correlation of records of $\delta^{13}C_{carb}$

The G-L CIE is characterized by a pronounced decrease in $\delta^{13}C$ values near the boundary[57]. Our $\delta^{13}C_{carb}$ profile exhibits trends and patterns that are consistent with those of other G-L records observed in various paleo-continental regions (Supplementary Fig. 2). This consistency suggests that the $\delta^{13}C_{carb}$ record from Shangsi reflects the typical marine $\delta^{13}C_{DIC}$ signal, which was subsequently used to calculate the isotopic composition of dissolved CO_2.

LOESS

The running average was generated using the locally estimated scatterplot smoothing (LOESS) function in SigmaPlot V14 software. For this calculation, a first-order polynomial was applied as the smoothing degree, and the sampling frequency was set to 0.4 to define the proportion of data points included in the smoothing process.

Estimating the impact of Maokou Formation weathering on the carbon cycle

Estimating the volume and mass of eroded Maokou limestone. The uplifted area of the Maokou Formation is approximately 2,010,619 km^2, assuming a circular area with a radius of 800 km (ref. 32). The estimated average erosion thickness is 150 m (ref. 32), resulting in an eroded volume of 301,593 km^3 (calculated as 2,010,619 km^2 × 0.15 km). With an average limestone density of 2.5 × 10^{12} kg/km^3, the total mass of the eroded limestone is calculated to be 7.54 × 10^{17} kg or 754,000 Gt.

Total organic carbon content in Maokou Formation samples. To evaluate the total organic carbon (TOC) content of the Maokou Formation, we compiled previously published TOC data from different sections. Reported average TOC values are 1.64% at Chaotian[86], 1.96% at Shangsi[87], 7.58% at Xibeixiang[88] and 0.19% at Tieqiao[89]. As the Xibeixiang data are limited to the uppermost Maokou Formation, they are excluded from subsequent analyses. The remaining three sections exhibit relatively consistent values, with a weighted average of 1.26% for the Maokou Formation. Note that the Shangsi value is taken from an independent study[87] rather than our own measurements; however, our TOC data yield a similar value (2.13%), supporting the reliability of the published result.

Limestones generally contain less organic carbon than fine-grained siliciclastic rocks (e.g., shales) deposited in the same settings. The TOC content in most marine limestones is relatively low, typically below 0.5%. Modern carbonate sediments can accumulate organic matter in amounts comparable to shales, but much of the organic carbon is lost during burial through oxidation or decay, resulting in only a small residual TOC. However, certain limestone units do display elevated TOC under some specific conditions, such as anoxic bottom waters, high primary productivity and rapid burial, which facilitate the formation of organic-rich limestones.

Widespread anoxic conditions during the deposition of the Maokou Formation have been documented across various regions, including mid- to high-latitude areas of Panthalassa and the Tethys Ocean[86,90–94]. These oxygen-deficient conditions were not restricted to deep marine basins but also extended into intermediate to shallow water depths[40,86,90–92,95]. For instance, sulfur ($\delta^{34}S$) isotope records coupled with pyrite iron speciation analyses from the shelf carbonates at Chaotian reveal that the expansion of the oxygen minimum zone (OMZ) during the Capitanian drove the development of euxinic conditions[86]. Similarly, multiple sulfur isotopes ($\delta^{34}S$ and $\Delta^{33}S$) in pyrites from the Penglaitan and Tieqiao sections further support the widespread shoaling of sulfidic waters[90]. Furthermore, negative shifts in $\delta^{238}U$ values of marine limestones at Xikou also suggest intensified marine anoxia, with an estimated ~10% anoxic seafloor coverage lasting >3 Myr (ref. 96). In addition, remarkably high nitrogen isotope values ($\delta^{15}N$ > 6‰, with peaks ≥ 10‰) in Maokou Formation limestones have been reported across several regions, exceeding most Phanerozoic $\delta^{15}N$ records[86,91,97–99]. In the modern deep ocean, nitrate $\delta^{15}N$ values typically range from 4‰ to 6‰. However, strongly denitrifying OMZs (e.g., the eastern tropical Pacific Ocean and the Arabian Sea) often exhibit exceptionally high $\delta^{15}N$ values of 15–20‰ (refs. 100,101). These regions with such high $\delta^{15}N$ values are characterized by high-productivity and low-oxygen levels, where intense water-column denitrification occurs. Therefore, these findings suggest that the Maokou Formation was likely deposited under oxygen-depleted conditions, which may have facilitated the accumulation of relatively high TOC in carbonate sediments.

Estimating the carbon content of eroded material. Inorganic carbon (carbonate): assuming a carbon content of 12% in $CaCO_3$, the mass of inorganic carbon is estimated at 90,480 Gt C (calculated as 754,000 Gt × 0.12). Organic carbon: the average total organic carbon content is 1.26 wt%, resulting in an estimated mass of organic carbon of 9,500.4 Gt C (calculated as 754,000 Gt × 0.0126).

Impact on the carbon cycle. Carbonate weathering involves the chemical reaction:

$$CaCO_3 + CO_2 + H_2O \rightarrow Ca^{2+} + 2HCO_3^- \quad (1)$$

and consumes 90,480 Gt of atmospheric CO_2. Conversely, organic carbon weathering occurs through the reaction:

$$CH_2O + O_2 \rightarrow CO_2 + H_2O \quad (2)$$

and releases 9,500.4 Gt C into the atmosphere. The net effect on the carbon cycle yields a net consumption of 80,979.6 Gt C. Over a period of 3 million years, this results in a rate of change of approximately 0.027 Gt C per year.

Impact on the marine carbonate $\delta^{13}C$. Assuming the $\delta^{13}C$ of weathered and original marine carbonate is approximately 0‰, and that of organic carbon is −25‰, the mass balance calculation for $\delta^{13}C$ of the total input gives $\delta^{13}C_{total}$ as (90,480 × 0‰ + 9500.4 × −25‰) / 99,980.4 = −2.375‰. Without buffering effects, the initial ocean carbon stands at 38,000 Gt C with a $\delta^{13}C$ of +1‰. After including the input from weathering, which totals 99,980.4 Gt C at −2.375‰, the new $\delta^{13}C$ calculates to (38,000 × 1‰ + 99,980.4 × −2.375‰) / 137,980.4 = −1.39‰. This suggests a potential negative shift in marine carbonate $\delta^{13}C$ of approximately 2.39‰, from +1‰ to −1.39‰, over a period of 3 million years.

Considering buffering, the carbonate compensation assumes that for every mole of CO_2 added from weathering, about 0.8 moles of carbonate sediment dissolve, totaling 99,980.4 Gt C × 0.8 = 79,984.32 Gt C. Assuming $\delta^{13}C$ of carbonate sediments similar to the initial ocean DIC at +1‰, a new mass balance calculation for the total carbon, which now amounts to 38,000 + 99,980.4 + 79,984.32 = 217,964.72 Gt C, yields a new $\delta^{13}C$ of (38,000 × 1‰ + 99,980.4 × −2.375‰ + 79,984.32 × 1‰) / 217,964.72 = −0.28‰. Thus, the buffered change in $\delta^{13}C$ equates to −0.28‰ from the initial +1‰, resulting in a change of −1.28‰.

Impact on the atmospheric CO_2. The initial Permian atmospheric CO_2 concentration was set to be 700 ppm. To convert this value into gigatons of carbon (Gt C), we assume the present-day atmospheric mass of 5.1 × 10^{18} kg and a molecular weight ratio of CO_2 to air of 1.52. Using these values, 700 ppm is equivalent to 700 × 5.1 × 10^{18} × 1.52 / (10^6 × 10^6) = 5426.4 Gt CO_2. Converting this to carbon, we yield 5426.4 Gt CO_2 × (12/44) = 1479.9 Gt C. Without buffering effects, the net consumption of 80,979.6 Gt C would far exceed the initial atmospheric CO_2 content of 1479.9 Gt C, indicating the potential for complete depletion of atmospheric CO_2. However, considering buffering

mechanisms such as carbonate compensation, we conservatively estimate that only 10% of the net change would affect the atmosphere. This results in 80,979.6 Gt C × 0.1 = 8097.96 Gt C net removal from the atmosphere, which still exceeds the initial atmospheric CO_2 content. A more realistic scenario might involve atmospheric CO_2 decreasing by approximately half, leading to a 1479.9 Gt C × 0.5 = 739.95 Gt C decrease. This would reduce the new atmospheric CO_2 level to 1479.9−739.95 = 739.95 Gt C. Converting this back to ppm, we find that 739.95 Gt C is equivalent to 2713.15 Gt CO_2. Using the same conversion factors, we estimate the new atmospheric CO_2 concentration to be approximately 350 ppm.

Sensitivity analysis of net CO_2 consumption. To assess robustness, we quantified how the carbonate-weathering sink scales with the geometry of the uplifted dome and the organic-carbon content by exploring dome radius of 600–900 km, average erosion thickness of 50–300 m, and bulk TOC values of 0.5–2 wt%. For all combinations, the net carbon sink ranges from 1.41×10^4 Gt C at (600 km, 50 m, 2%) to 2.19×10^5 Gt C at (900 km, 300 m, 0.5%), and is therefore $\gg 10^3$ Gt C under all tested conditions (Supplementary Fig. 6). Assuming a 2–4 Myr weathering interval, mean removal rates span 0.003–0.11 Gt C yr^{-1}. Note that our estimate of the carbonate-weathering volume and rate represents a simplified, first-order approximation intended to illustrate the likely range of values rather than capture the full complexity of the system.

In summary, the weathering of the Maokou Formation over a 3-million-year period likely had significant impacts on the global carbon cycle. The weathering process could have caused a substantial negative shift in marine carbonate $\delta^{13}C$, potentially up to −2.39‰ without buffering effects. When considering buffering, the shift is estimated to be around −1.28‰, which remains significant and detectable in the geological record. This could have had important implications for marine ecosystems and carbon cycling. Additionally, a significant drawdown of atmospheric CO_2 is predicted, with levels potentially decreasing from 700 ppm to approximately 350 ppm, even after accounting for buffering effects. This substantial decrease in CO_2 would likely have had significant climatic implications in the lead-up to the Emeishan volcanism event.

The actual magnitude of these effects, however, would depend on several factors, including ocean chemistry, biological feedbacks, and the precise operation of the carbon cycle in the Permian period. Nonetheless, the estimated changes align with emerging geological evidence, supporting the hypothesis that pre-LIP mantle-crustal processes significantly impacted the carbon cycle and global environment during this period.

Data availability

All data that support the findings of this study have been deposited in the Figshare repository at https://doi.org/10.6084/m9.figshare.30812294 (ref. 102).

Code availability

Code used to perform Monte Carlo Simulations can be accessed at https://doi.org/10.6084/m9.figshare.29094035 (ref. 103).

References

1. Coffin, M. F. & Eldholm, O. Large igneous provinces: crustal structure, dimensions, and external consequences. *Rev. Geophys.* **32**, 1–36 (1994).
2. Wignall, P. B. Large igneous provinces and mass extinctions. *Earth-Sci. Rev.* **53**, 1–33 (2001).
3. Royer, D. L., Berner, R. A., Montañez, I. P., Tabor, N. J. & Beerling, D. J. CO2 as a primary driver of Phanerozoic climate. *GSA Today* **14**, 3–7 (2004).
4. Schaller, M. F., Wright, J. D. & Kent, D. V. Atmospheric Pco2 perturbations associated with the central atlantic magmatic province. *Science* **331**, 1404–1409 (2011).
5. Tian, X. & Buck, W. R. Intrusions induce global warming before continental flood basalt volcanism. *Nat. Geosci.* **15**, 417–422 (2022).
6. Black, B. A. et al. Cryptic degassing and protracted greenhouse climates after flood basalt events. *Nat. Geosci.* **17**, 1162–1168 (2024).
7. Stanley, S. M. & Yang, X. A double mass extinction at the end of the Paleozoic era. *Science* **266**, 1340–1344 (1994).
8. Fan, J. -x et al. A high-resolution summary of Cambrian to Early Triassic marine invertebrate biodiversity. *Science* **367**, 272–277 (2020).
9. Groves, J. R. & Wang, Y. Timing and size selectivity of the Guadalupian (Middle Permian) fusulinoidean extinction. *J. Paleontol.* **87**, 183–196 (2013).
10. Wang, X. D. & Sugiyama, T. Diversity and extinction patterns of Permian coral faunas of China. *Lethaia* **33**, 285–294 (2000).
11. Shen, S.-Z. & Shi, G. R. Latest Guadalupian brachiopods from the Guadalupian/Lopingian boundary GSSP section at Penglaitan in Laibin, Guangxi, South China and implications for the timing of the pre-Lopingian crisis. *Palaeoworld* **18**, 152–161 (2009).
12. Bond, D. P. G. et al. The Middle Permian (Capitanian) mass extinction on land and in the oceans. *Earth-Sci. Rev.* **102**, 100–116 (2010).
13. Chen, J. & Shen, S. in *Encyclopedia of Geology (Second Edition)* (eds David Alderton & Scott A. Elias) 637–644 (Academic Press, 2021).
14. Chen, J. & Xu, Y. -g Establishing the link between Permian volcanism and biodiversity changes: Insights from geochemical proxies. *Gondwana Res.* **75**, 68–96 (2019).
15. Zhong, Y.-T., He, B., Mundil, R. & Xu, Y.-G. CA-TIMS zircon U–Pb dating of felsic ignimbrite from the Binchuan section: Implications for the termination age of Emeishan large igneous province. *Lithos* **204**, 14–19 (2014).
16. Zhong, Y. et al. Geochemical, biostratigraphic, and high-resolution geochronological constraints on the waning stage of Emeishan Large Igneous Province. *GSA Bull.* **132**, 1969–1986 (2020).
17. Huang, H. et al. Eruptive tempo of Emeishan large igneous province, southwestern China and northern Vietnam: Relations to biotic crises and paleoclimate changes around the Guadalupian-Lopingian boundary. *Geology* **50**, 1083–1087 (2022).
18. Zhou, M.-F. et al. A temporal link between the Emeishan large igneous province (SW China) and the end-Guadalupian mass extinction. *Earth Planet. Sci. Lett.* **196**, 113–122 (2002).
19. Huang, Y. et al. Biotic responses to volatile volcanism and environmental stresses over the Guadalupian-Lopingian (Permian) transition. *Geology* **47**, 175–178 (2018).
20. Rontani, J.-F. & Volkman, J. K. Phytol degradation products as biogeochemical tracers in aquatic environments. *Org. Geochem.* **34**, 1–35 (2003).
21. Naafs, B. D. A. et al. Gradual and sustained carbon dioxide release during Aptian Oceanic Anoxic Event 1a. *Nat. Geosci.* **9**, 135–139 (2016).
22. Witkowski, C. R., Weijers, J. W. H., Blais, B., Schouten, S. & Sinninghe Damsté, J. S. Molecular fossils from phytoplankton reveal secular Pco2 trend over the Phanerozoic. *Sci. Adv.* **4**, eaat4556 (2018).
23. Shen, J., Zhang, Y. G., Yang, H., Xie, S. & Pearson, A. Early and late phases of the Permian–Triassic mass extinction marked by different atmospheric CO2 regimes. *Nat. Geosci.* **15**, 839–844 (2022).
24. Graham, O. A., Witkowski, C. R., Stevenson, M. A., Peterse, F. & Naafs, D. A. A. phytol εp-based core-top calibration to reconstruct past changes in atmospheric CO2. *Geochimica Et. Cosmochimica Acta* **398**, 178–192 (2025).

25. Freeman, K. H. & Hayes, J. M. Fractionation of carbon isotopes by phytoplankton and estimates of ancient CO2 levels. *Glob. Biogeochem. Cycles* **6**, 185–198 (1992).
26. Laws, E. A., Popp, B. N., Bidigare, R. R., Kennicutt, M. C. & Macko, S. A. Dependence of phytoplankton carbon isotopic composition on growth rate and [CO2)aq: theoretical considerations and experimental results. *Geochimica et. Cosmochimica Acta* **59**, 1131–1138 (1995).
27. Popp, B. N. et al. Effect of phytoplankton cell geometry on carbon isotopic fractionation. *Geochimica et. Cosmochimica Acta* **62**, 69–77 (1998).
28. Zhang, Y. G., Henderiks, J. & Liu, X. Refining the alkenone-pCO2 method II: towards resolving the physiological parameter 'b'. *Geochimica et. Cosmochimica Acta* **281**, 118–134 (2020).
29. Shellnutt, J. G., Pham, T. T., Denyszyn, S. W., Yeh, M.-W. & Tran, T.-A. Magmatic duration of the Emeishan large igneous province: insight from northern Vietnam. *Geology* **48**, 457–461 (2020).
30. Gutjahr, M. et al. Very large release of mostly volcanic carbon during the Palaeocene–Eocene Thermal Maximum. *Nature* **548**, 573–577 (2017).
31. Wu, Y. et al. Six-fold increase of atmospheric pCO2 during the Permian–Triassic mass extinction. *Nat. Commun.* **12**, 2137 (2021).
32. He, B., Xu, Y.-G., Chung, S.-L., Xiao, L. & Wang, Y. Sedimentary evidence for a rapid, kilometer-scale crustal doming prior to the eruption of the Emeishan flood basalts. *Earth Planet. Sci. Lett.* **213**, 391–405 (2003).
33. He, B., Xu, Y.-G., Guan, J.-P. & Zhong, Y.-T. Paleokarst on the top of the Maokou Formation: Further evidence for domal crustal uplift prior to the Emeishan flood volcanism. *Lithos* **119**, 1–9 (2010).
34. Xu, Y.-G., He, B., Chung, S.-L., Menzies, M. A. & Frey, F. A. Geologic, geochemical, and geophysical consequences of plume involvement in the Emeishan flood-basalt province. *Geology* **32**, 917–920 (2004).
35. Campbell, I. H. & Griffiths, R. W. Implications of mantle plume structure for the evolution of flood basalts. *Earth Planet. Sci. Lett.* **99**, 79–93 (1990).
36. Griffiths, R. W. & Campbell, I. H. Interaction of mantle plume heads with the Earth's surface and onset of small-scale convection. *J. Geophys. Res. Solid Earth* **96**, 18295–18310 (1991).
37. Farnetani, C. G. & Richards, M. A. Numerical investigations of the mantle plume initiation model for flood basalt events. *J. Geophys. Res. Solid Earth* **99**, 13813–13833 (1994).
38. Cao, C. et al. Persistent late Permian to Early Triassic warmth linked to enhanced reverse weathering. *Nat. Geosci.* **15**, 832–838 (2022).
39. Sun, S. et al. Rapid climatic fluctuations during the Guadalupian-Lopingian transition: Implications from weathering indices recorded in acid-insoluble residues of carbonate rocks, South China. *J. Asian Earth Sci.* **230**, 105222 (2022).
40. Zhang, B., Wignall, P. B., Yao, S., Hu, W. & Liu, B. Collapsed upwelling and intensified euxinia in response to climate warming during the Capitanian (Middle Permian) mass extinction. *Gondwana Res.* **89**, 31–46 (2021).
41. Marcilly, C. M., Torsvik, T. H. & Jones, M. T. Late Paleozoic climate transition from a long-term carbon cycle modeling perspective. *Global and Planetary Change* **253**, 104984 (2025).
42. Goddéris, Y. et al. Onset and ending of the late Palaeozoic ice age triggered by tectonically paced rock weathering. *Nat. Geosci.* **10**, 382–38 (2017).
43. Berner, R. A. & Kothavala, Z. GEOCARB III: a revised model of atmospheric CO 2 over Phanerozoic time. *Am. J. Sci.* **301**, 182–204 (2001).
44. Ridgwell, A. & Zeebe, R. E. The role of the global carbonate cycle in the regulation and evolution of the Earth system. *Earth Planet. Sci. Lett.* **234**, 299–315 (2005).
45. Tang, Q. et al. The origin of volatiles in the Emeishan large igneous province, China: constraints from chemical and C–He–Ar isotopic compositions of volatiles in picrites and basalts. *Geol. J.* **56**, 3626–3643 (2021).
46. Svensen, H. et al. Siberian gas venting and the end-Permian environmental crisis. *Earth Planet. Sci. Lett.* **277**, 490–500 (2009).
47. Svensen, H. H. et al. Sills and gas generation in the Siberian Traps. *Philosoph. Trans. R. Soc. a-Math. Phys. Eng. Sci.* **376**, 20170080 (2018).
48. Svensen, H. H., Jones, M. T. & Mather, T. A. Large igneous provinces and the release of thermogenic volatiles from sedimentary basins. *Elements* **19**, 282–288 (2023).
49. Burgess, S. D., Muirhead, J. D. & Bowring, S. A. Initial pulse of Siberian Traps sills as the trigger of the end-Permian mass extinction. *Nat. Commun.* **8**, 164 (2017).
50. Jones, M. T., Jerram, D. A., Svensen, H. H. & Grove, C. The effects of large igneous provinces on the global carbon and sulphur cycles. *Palaeogeogr. Palaeoclimatol. Palaeoecol.* **441**, 4–21 (2016).
51. Burgess, S. D. & Bowring, S. A. High-precision geochronology confirms voluminous magmatism before, during, and after Earth's most severe extinction. *Science Advances* **1**, e1500470 (2015).
52. Zhou, M. F. et al. Geochemistry, petrogenesis and metallogenesis of the Panzhihua gabbroic layered intrusion and associated Fe-Ti-V oxide deposits, Sichuan Province, SW China. *J. Petrol.* **46**, 2253–2280 (2005).
53. Zhong, H. & Zhu, W. G. Geochronology of layered mafic intrusions from the Pan-Xi area in the Emeishan large igneous province, SW China. *Mineralium Depos.* **41**, 599–606 (2006).
54. Zhong, H. et al. Timing and source constraints on the relationship between mafic and felsic intrusions in the Emeishan large igneous province. *Geochimica Et. Cosmochimica Acta* **75**, 1374–1395 (2011).
55. Ganino, C. & Arndt, N. T. Climate changes caused by degassing of sediments during the emplacement of large igneous provinces. *Geology* **37**, 323–326 (2009).
56. Yuan, D.-X. et al. Integrative timescale for the Lopingian (Late Permian): a review and update from Shangsi, South China. *Earth-Sci. Rev.* **188**, 190–209 (2019).
57. Shen, S. -z. et al. Progress, problems and prospects: an overview of the Guadalupian Series of South China and North America. *Earth-Sci. Rev.* **211**, 103412 (2020).
58. Wu, Q. et al. High-precision U-Pb zircon age constraints on the Guadalupian in West Texas, USA. *Palaeogeogr. Palaeoclimatol. Palaeoecol.* **548**, 109668 (2020).
59. Yang, J. et al. Early Wuchiapingian cooling linked to Emeishan basaltic weathering? *Earth Planet. Sci. Lett.* **492**, 102–111 (2018).
60. Shen, S. -z. et al. Calibrating the end-permian mass extinction. *Science* **334**, 1367–1372 (2011).
61. Shellnutt, J. G. et al. Three Fe-Ti oxide ore-bearing gabbro-granitoid complexes in the Panxi region of the Permian Emeishan Large Igneous Province, SW China. *Am. J. Sci.* **311**, 773–812 (2011).
62. Chen, Y. et al. Magmatic underplating and crustal growth in the Emeishan Large Igneous Province, SW China, revealed by a passive seismic experiment. *Earth Planet. Sci. Lett.* **432**, 103–114 (2015).
63. Huang, Y., He, C., Chen, N. S. & Xia, B. Diabase sills in the outer zone of the emeishan large igneous province, Southwest China: petrogenesis and tectonic implications. *J. Earth Sci.* **30**, 739–753 (2019).
64. Tang, Q. et al. Sr-Nd-Hf-O isotope constraints on crustal contamination and mantle source variation of three Fe-Ti-V oxide ore deposits in the Emeishan large igneous province. *Geochimica et. Cosmochimica Acta* **292**, 364–381 (2021).
65. Ganino, C., Arndt, N. T., Chauvel, C., Jean, A. & Athurion, C. Melting of carbonate wall rocks and formation of the

heterogeneous aureole of the Panzhihua intrusion, China. *Geosci. Front.* **4**, 535–546 (2013).
66. Ganino, C., Arndt, N. T., Zhou, M. F., Gaillard, F. & Chauvel, C. Interaction of magma with sedimentary wall rock and magnetite ore genesis in the Panzhihua mafic intrusion, SW China. *Mineralium Depos.* **43**, 677–694 (2008).
67. Shen, J. et al. Improved efficiency of the biological pump as a trigger for the Late Ordovician glaciation. *Nat. Geosci.* **11**, 510–514 (2018).
68. Meyers, P. A. Organic geochemical proxies of paleoceanographic, paleolimnologic, and paleoclimatic processes. *Org. Geochem.* **27**, 213–250 (1997).
69. Bray, E. E. & Evans, E. D. Distribution of n-paraffins as a clue to recognition of source beds. *Geochimica et. Cosmochimica Acta* **22**, 2–15 (1961).
70. Peters, K. E., Walters, C. C. & Moldowan, J. M. *The Biomarker Guide: Volume 2: Biomarkers and Isotopes in Petroleum Systems and Earth History*. 2 edn, Vol. 2 (Cambridge University Press, 2004).
71. Hughes, W. B., Holba, A. G. & Dzou, L. I. P. The ratios of dibenzothiophene to phenanthrene and pristane to phytane as indicators of depositional environment and lithology of petroleum source rocks. *Geochimica Et. Cosmochimica Acta* **59**, 3581–3598 (1995).
72. Mook, W. G., Bommerson, J. C. & Staverman, W. H. Carbon isotope fractionation between dissolved bicarbonate and gaseous carbon dioxide. *Earth Planet. Sci. Lett.* **22**, 169–176 (1974).
73. Romanek, C. S., Grossman, E. L. & Morse, J. W. Carbon isotopic fractionation in synthetic aragonite and calcite: Effects of temperature and precipitation rate. *Geochimica et. Cosmochimica Acta* **56**, 419–430 (1992).
74. Chen, B., Joachimski, M. M., Sun, Y., Shen, S. & Lai, X. Carbon and conodont apatite oxygen isotope records of Guadalupian–Lopingian boundary sections: climatic or sea-level signal? *Palaeogeography. Palaeoclimatol. Palaeoecol.* **311**, 145–153 (2011).
75. Chen, B. et al. Permian ice volume and palaeoclimate history: oxygen isotope proxies revisited. *Gondwana Res.* **24**, 77–89 (2013).
76. Farquhar, G. D., Ehleringer, J. R. & Hubick, K. T. Carbon isotope discrimination and photosynthesis. *Annu. Rev. Plant Physiol. Plant Mol. Biol.* **40**, 503–537 (1989).
77. Giordano, M., Beardall, J. & Raven, J. A. CO2 concentrating mechanisms in algae: mechanisms, environmental modulation, and evolution. *Annu. Rev. Plant Biol.* **56**, 99–131 (2005).
78. Jasper, J. P. & Hayes, J. M. A carbon isotope record of CO2 levels during the late Quaternary. *Nature* **347**, 462–464 (1990).
79. Goericke, R. Physiology of isotopic fractionation in algae and cyanobacteria. *Stable Isotopes in Ecology Environmental Science*, 187–221 (Blackwell Scientific Publications, 1994).
80. Bidigare, R. R. et al. Consistent fractionation of 13C in nature and in the laboratory: growth-rate effects in some haptophyte algae. *Glob. Biogeochem. Cycles* **11**, 279–292 (1997).
81. Weiss, R. F. Carbon dioxide in water and seawater: the solubility of a non-ideal gas. *Mar. Chem.* **2**, 203–215 (1974).
82. Zhang, Y. G. et al. Refining the alkenone-pCO2 method I: lessons from the quaternary glacial cycles. *Geochimica et. Cosmochimica Acta* **260**, 177–191 (2019).
83. Raven, J. A. & Johnston, A. M. Mechanisms of inorganic-carbon acquisition in marine phytoplankton and their implications for the use of other resources. *Limnol. Oceanogr.* **36**, 1701–1714 (1991).
84. Wilkes, E. B., Carter, S. J. & Pearson, A. CO2-dependent carbon isotope fractionation in the dinoflagellate Alexandrium tamarense. *Geochimica et. Cosmochimica Acta* **212**, 48–61 (2017).
85. Pagani, M. et al. The role of carbon dioxide during the onset of Antarctic glaciation. *Science* **334**, 1261–1264 (2011).
86. Saitoh, M. et al. Isotopic evidence for water-column denitrification and sulfate reduction at the end-Guadalupian (Middle Permian). *Glob. Planet. Change* **123**, 110–120 (2014).
87. Wang, Y. et al. Coupled volcanic activity and marine anoxia in the Upper Yangtze region prior to the Capitanian mass extinction. *Chem. Geol.* **644**, 121838 (2024).
88. Pang, Q. et al. Extraordinarily high organic matter enrichment during the late Guadalupian in northwestern Sichuan basin, China. *J. Pet. Sci. Eng.* **210**, 110058 (2022).
89. Yan, D., Zhang, L. & Qiu, Z. Carbon and sulfur isotopic fluctuations associated with the end-Guadalupian mass extinction in South China. *Gondwana Res.* **24**, 1276–1282 (2013).
90. Zhang, G. et al. Widespread shoaling of sulfidic waters linked to the end-Guadalupian (Permian) mass extinction. *Geology* **43**, 1091–1094 (2015).
91. Schoepfer, S. D. et al. Termination of a continent-margin upwelling system at the Permian–Triassic boundary (Opal Creek, Alberta, Canada). *Glob. Planet. Change* **105**, 21–35 (2013).
92. Isozaki, Y. Permo-Triassic boundary superanoxia and stratified superocean: records from lost deep sea. *Science* **276**, 235–238 (1997).
93. Bond, D. P. G. et al. An abrupt extinction in the Middle Permian (Capitanian) of the Boreal Realm (Spitsbergen) and its link to anoxia and acidification. *GSA Bull.* **127**, 1411–1421 (2015).
94. Bond, D. P. G., Wignall, P. B. & Grasby, S. E. The Capitanian (Guadalupian, Middle Permian) mass extinction in NW Pangea (Borup Fiord, Arctic Canada): a global crisis driven by volcanism and anoxia. *GSA Bull.* **132**, 931–942 (2019).
95. Smith, B. P., Larson, T., Martindale, R. C. & Kerans, C. Impacts of basin restriction on geochemistry and extinction patterns: a case from the Guadalupian Delaware Basin, USA. *Earth Planet. Sci. Lett.* **530**, 115876 (2020).
96. Wang, W. -q. et al. Ecosystem responses of two Permian biocrises modulated by CO2 emission rates. *Earth Planet. Sci. Lett.* **602**, 117940 (2023).
97. Schoepfer, S. D., Henderson, C. M., Garrison, G. H. & Ward, P. D. Cessation of a productive coastal upwelling system in the Panthalassic Ocean at the Permian–Triassic Boundary. *Palaeogeogr. Palaeoclimatol. Palaeoecol.* **313-314**, 181–188 (2012).
98. Grasby, S. E. et al. Global warming leads to Early Triassic nutrient stress across northern Pangea. *GSA Bull.* **132**, 943–954 (2019).
99. Algeo, T. J., Meyers, P. A., Robinson, R. S., Rowe, H. & Jiang, G. Q. Icehouse–greenhouse variations in marine denitrification. *Biogeosciences* **11**, 1273–1295 (2014).
100. Brandes, J. A., Devol, A. H., Yoshinari, T., Jayakumar, D. A. & Naqvi, S. W. A. Isotopic composition of nitrate in the central Arabian Sea and eastern tropical North Pacific: a tracer for mixing and nitrogen cycles. *Limnol. Oceanogr.* **43**, 1680–1689 (1998).
101. Voss, M., Dippner, J. W. & Montoya, J. P. Nitrogen isotope patterns in the oxygen-deficient waters of the Eastern Tropical North Pacific Ocean. *Deep Sea Res. Part I Oceanogr. Res. Pap.* **48**, 1905–1921 (2001).
102. Huang, Y. et al. Restoration of reef ecosystems following the Guadalupian–Lopingian boundary mass extinction: Evidence from the Laibin area, South China. *Palaeogeogr. Palaeoclimatol. Palaeoecol.* **519**, 8–22 (2019).
103. Shen, J. GLB Dataset. *Figshare* https://doi.org/10.6084/m9.figshare.30812294.v1 (2025).
104. Shen, J. GLB Monte Carlo Simulations. *Figshare* https://doi.org/10.6084/m9.figshare.29094035.v1 (2025)

Acknowledgements
We sincerely thank Xiaoyan Ruan and Xinbo Gao for their assistance with field work; Liping Zhou, Shiling Yang, Linlin Cui and Han Zhang for generously providing laboratory space and support with isotopic analyses; Ann Pearson for providing isotopic standards; and Yuting Zhong for insightful discussions on the geochronological data of the Emeishan LIP. Funding: This work was supported by the National Natural Science Foundation of China (Grants No. 42220104003 and 42488201 to J.S.). Y.-G.X. was funded by the National Natural Science Foundation of China (Grant No. 92479001). D.-X.Y. received support from the National Natural Science Foundation of China (Grant No. 42272031).

Author contributions
J.S. conceived the study and performed the biomarker/bulk sediment analyses. J.S., Y.G.Z., and Y.-G.X. interpreted the data. J.S. and D.-X.Y. carried out the stratigraphic work. J.S. wrote the initial manuscript. Y.G.Z. revised the text, with additional edits from Y.-G.X. and D.-X.Y.

Competing interests
The authors declare no competing interests.

Additional information
Supplementary information The online version contains supplementary material available at https://doi.org/10.1038/s41467-026-69600-z.

Correspondence and requests for materials should be addressed to Jiaheng Shen.

Peer review information *Nature Communications* thanks the anonymous reviewer(s) for their contribution to the peer review of this work. A peer review file is available.